ACS OMEGA

Article

Cite This: ACS Omega 2019, 4, 11455−11463

http://pubs.acs.org/journal/acsodf

Enhanced Hybrid Capacitive Deionization Performance by Sodium Titanium Phosphate/Reduced Porous Graphene Oxide Composites

Cuilian Han,[†] Qinghan Meng,*[,†] Bing Cao,[†] and Guiying Tian*[,‡]

[†]College of Materials Science and Engineering, Beijing University of Chemical Technology (BUCT), Beijing 100029, China

[‡]Institute for Applied Materials (IAM), Karlsruhe Institute of Technology (KIT), Hermann-von-Helmholtz-Platz 1, Eggenstein-Leopoldshafen 76344, Germany

ABSTRACT: In this study, sodium titanium phosphate/reduced porous graphene oxide (NTP/rPGO) composites are used as novel electrode materials for hybrid capacitive deionization (HCDI). The composites are synthesized through assembling the $NaTi_2(PO_4)_3$ precursor with etched graphene oxide under hydrothermal condition. The NTP/rPGO composites demonstrate a porous hierarchical structure, where uniformly dispersed $NaTi_2(PO_4)_3$ particles are attached on the rPGO sheets, which provide abundant adsorption sites, highly conductive networks, and short diffusion lengths for salt ions. Benefiting from the redox reaction of the NTP and electrical double-layer capacity of the rPGO, the NTP/rPGO composite containing 77 wt % $NaTi_2(PO_4)_3$ presents a high specific capacity of 396.42 F g^{-1} and a high electrosorption capacity of 33.25 mg g^{-1} at the voltage of 1.4 V with the initial salt conductivity of 1600 μS cm^{-1} (786 mg L^{-1}). Further, it also shows excellent recycling stability and rapid desalination rate of 0.30 mg g^{-1} s^{-1} (100 times as fast as the bare graphene electrode). Therefore, the NTP/rPGO composites exhibit a promising prospect for desalination application in the HCDI system.

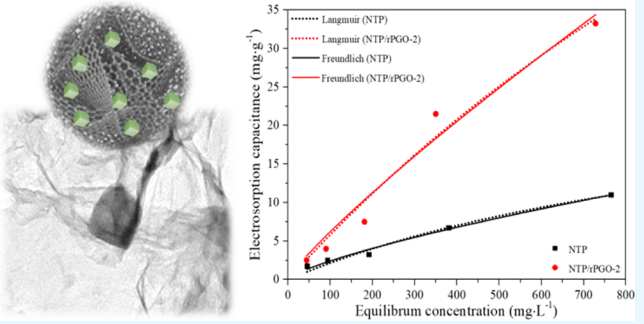

1. INTRODUCTION

Recently, the ever-increasing demand for fresh water is a huge challenge due to population explosion, industrial consumption, and environmental contamination. This encouraged the rapid development of water desalination technologies in a cost-effective and energy-efficient direction.[1,2] However, current technologies used in the desalination (e.g., reverse osmosis and thermal distillation) exhibit obvious drawbacks, such as high energy consumption, secondary pollution, and high operation costs.[3−5] Instead, capacitive deionization (CDI), known as electrosorptive desalination, is considered as a cost-effective desalination method due to its easy operation, low energy consumption, and high sustainability.[6−9] However, the CDI still faces some intrinsic limitations. Salt ions can only store at the surface of the electrodes based on the electrical double layer (EDL) mechanism.[10,11] In addition, counterions can be straightly adsorbed on the opposite electrode when a reversed voltage is applied for the electrode regeneration.[12] To improve the desalination capacity for the practical application, a variety of derivation CDI techniques such as membrane capacitive deionization,[13,14] ion-exchange resin-coated CDI,[15] flow-electrode capacitive deionization,[16,17] inverted capacitive deionization,[18,19] desalination batteries,[20,21] and hybrid capacitive deionization (HCDI)[22] have been proposed. Among them, the HCDI shows an excellent deionization capacity compared to the conventional CDI and have attracted much attention.

As an asymmetric system, the HCDI consists of two types of electrodes: a capacitive electrode from conventional CDI system and a redox electrode from battery desalination system. In detail, the capacitive electrode shares the same mechanism for ion storage with supercapacitors. Therefore, carbon materials for the EDL capacitive electrode require high surface area, proper pore size distribution, enough surface wettability, and high conductivity.[23] To achieve these properties, various carbide materials have been investigated for capacitive deionization, such as activated carbon (AC),[24,25] carbon aerogel,[26,27] carbon nanotube,[28,29] carbon nanosheet,[30] and graphene.[31−33] On the other hand, the salt ions can be stored through the redox reaction in the battery-type electrode, which contributes to the high electrical capacity and desalination capacity, like Ag-coated carbon,[34] Co_3O_4,[35] $Na_4Mn_9O_{18}$,[22] and $Na_4Ti_9O_{20}$.[36] Given that Na^+ is the main ion in the seawater, the electrodes for sodium-ion batteries are expected to be applied in the HCDI system. Huang et al. applied the $NaTi_2(PO_4)_3$/rGO composite for electrochemical deionization, exhibiting high removal capacity of 27 mg g^{-1}.[37] However, slow reaction kinetics of intercalation can lead to a low desalination rate. Increase in the content of porous carbon in the $NaTi_2(PO_4)_3$ composites is a promising way to solve this issue. In addition, the porous conductive structure in the

Received: April 6, 2019
Accepted: June 21, 2019
Published: July 1, 2019

DOI: 10.1021/acsomega.9b00984
ACS Omega 2019, 4, 11455−11463

battery-type electrode can also enhance the electron conductivity and accommodate volume variation during the desalination process.

To modify the aforementioned problems, a suitable conductive substrate is highly expected to compose electrode materials. Due to the high specific surface area, superior mechanical property, and electrochemical performance, graphene (or reduced graphene oxide (rGO)) is intensively studied as an energy-storage material.[38] Some researchers attempted to create nanoholes on the graphene sheets to improve the electrochemical performance of the supercapacitors. For example, Xu et al. synthesized the porous graphene oxide (PGO) with abundant in-plane nanopores via a convenient defect-etching reaction, which showed excellent rate capabilities and cycling stability.[39] Therefore, the PGO sheets serving as building blocks provide a unique platform for designing novel electrode materials. To further improve the conductivity, a strategy is to design two-dimensional graphene sheets for the porous three-dimensional (3D) substrate, which is appealing to facilitate ion/electron migration and release volume change during the desalination process.

In this study, a porous 3D $NaTi_2(PO_4)_3$/reduced porous graphene oxide (NTP/rPGO) composites are fabricated via a hydrothermal method, followed by carbonization treatment, where the sodium titanium phosphate (NTP) particles are uniformly dispersed in the rPGO sheets. The hierarchical structure provides abundant adsorption sites and short diffusion lengths for salt ion transfer. An HCDI cell using the NTP/rPGO and activated carbon (AC) is assembled in this work, and desalination performances based on different electrochemical potentials, flow rates, and initial salt concentrations are also discussed in detail.

2. EXPERIMENTAL SECTION

2.1. Synthesis of the PGO and the NTP. First, GO was prepared with a modified Hummer method.[40] Afterward, a typical synthesis route of the PGO is described as follows: 5 mL of H_2O_2 (Beijing Chemical Works, 30%) aqueous solution was mixed with 50 mL of GO aqueous suspension (solid content of 2 mg mL^{-1}), and then the mixture was heated at 100 °C for 2 h. After centrifuging and washing steps to remove the residual H_2O_2, the mixture was dispersed in deionized water again to form a homogeneous PGO aqueous suspension, and the solid content was controlled to be 2 mg mL^{-1}.

Two millimolar of sodium acetate (CH_3COONa, Beijing Chemical, ≥99.0%) and 2 mmol of titanium butoxide ($Ti(OCH_2CH_2CH_2CH_3)_4$, Tianjin Damao Chemical, ≥99.0%) were dissolved into 6 mL of phosphorous acid (H_3PO_3, Beijing Chemical, 85%) solution and 40 mL of ethanol solvent, respectively. The mixture was mixed and then transferred into a 100 mL Teflon-lined autoclave for solvothermal reaction for 3 h at 160 °C. After cooling down to room temperature, the white product was washed with deionized water using centrifugation treatment. To stabilize the NTP precursor, the product was dispersed in deionized water again. When using for further steps, the NTP nanoparticles were obtained by drying at 80 °C and annealing at 700 °C for 2 h in N_2 flow.

2.2. Synthesis of the NTP/rPGO. NTP precursor, 0.2 g, without annealing treatment was added to the obtained PGO suspension (50, 75, and 100 mL, respectively) by magnetic stirring and ultrasonic treatment. Then, the solution was transferred into a Teflon-lined autoclave for hydrothermal reaction at 180 °C for 12 h. After washing, the gel-like product was freeze-dried and then annealed at 700 °C for 2 h in N_2 flow. The obtained NTP/rPGO composites were denoted as NTP/rPGO-1, NTP/rPGO-2, and NTP/rPGO-3, respectively, according to different volumes of the rPGO suspension (from low to high).

2.3. General Characterization. The morphology of the samples was characterized by scanning electron microscope (SEM, JSM7800F JEOL) and transmission electron microscope (TEM, HT7700 Hitachi). The crystal structure was analyzed by X-ray powder diffraction (XRD, advance D8 Bruker) using Cu $K\alpha_1$ radiation (λ = 1.54056 Å) in the 2θ range from 5 to 90°. The chemical information of the structure was characterized using Fourier transform infrared spectroscopy (FTIR, PerkinElmer Spectrum RX1). Raman test was measured at room temperature using a Renishaw in Via Raman system equipped with a 514 nm laser source. Thermal stability of the samples was analyzed using a thermogravimetry (TGA)/differential scanning calorimetry analyzer (Mettler Toledo) under air atmosphere with a heating rate of 10 °C min^{-1}. The N_2 adsorption−desorption isotherms were measured at 77 K (SPECTOMETER 1990, American Thermo), and the surface areas were calculated based on the Brunauer−Emmett−Teller (BET) method.

2.4. Electrochemical Test. Cyclic voltammetry (CV) and electrochemical impedance spectroscopy (EIS) measurements were carried out using an electrochemical workstation (Zennium, ZAHNER-elektrik), and a three-electrode system with 1 M Na_2SO_4 aqueous solution as an electrolyte was used here. The NTP/rPGO and activated carbon (AC) were used as working electrodes; a platinum plate and a saturated calomel electrode (SCE) were employed as a counter electrode and a reference electrode, respectively. The specific capacity (C_s) was calculated according to eq 1

$$C_s = A/(2v \times \Delta V \times m) \quad (1)$$

where A is the integral area in the CV curve, v is the scan rate (mV s^{-1}), ΔV is the potential window (V), and m is the loading mass (g) of active materials.

The deionization test was conducted in a recycling system, consisting of a self-made HCDI cell,[41] a conductometer (DDSJ-308A, Feilo Co., Ltd.), a peristaltic pump (BT100-2J, Longer Precision Pump Co., Ltd), and an Arbin battery test system. A typical electrode slurry was prepared by mixing active materials, acetylene black (Pengxiang Yunda Tech. CO., LTD., ≥99.7%), and poly(tetrafluoroethylene) (Shanghai Aladdin, 60.0%) in a mass ratio of 80:15:5. The active mass loading for each electrode is about 200 mg, with the coating area of 4 × 6 cm^2. NaCl aqueous solution with initial conductivity of 100−1600 μS cm^{-1} (or initial concentration of 49−786 mg L^{-1}, which mimics that of the seawater) was circularly pumped into the HCDI cell at different flow rates (20−40 mL min^{-1}) under constant potentials (1.0−1.4 V). The feeding volume and the solution temperature were maintained at 200 mL and 25 °C, respectively. The electrosorption capacity (S_c) of the electrode was calculated according to eq 2

$$S_c = (C_0 - C_f) \times V/m \quad (2)$$

where C_0 (mg L^{-1}) and C_f (mg L^{-1}) are the initial and the final concentrations of NaCl solution, respectively; V (L) is the volume of NaCl solution; and m (g) is the total active mass of both electrodes.

DOI: 10.1021/acsomega.9b00984
ACS Omega 2019, 4, 11455−11463

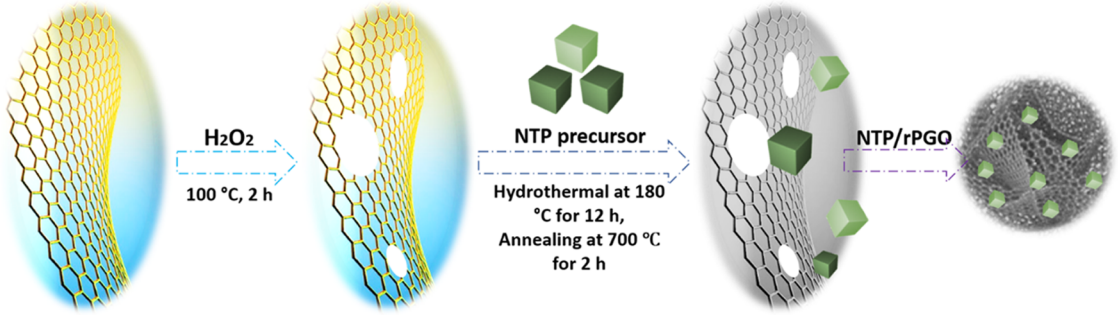

Figure 1. Schematic illustration of the synthesis process of the NTP/rPGO composites.

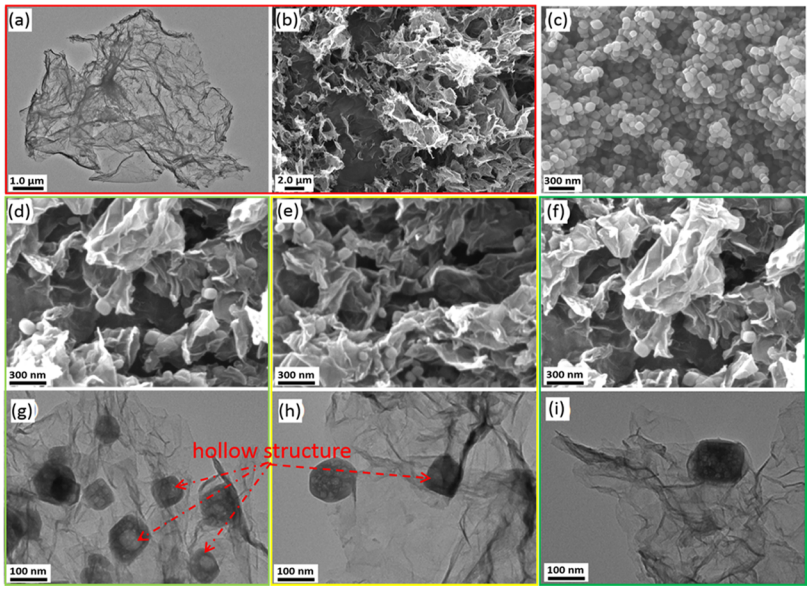

Figure 2. Morphological characterization: (a) TEM and (b) SEM images of the rPGO; (c) SEM images of the NTP; (d) TEM and (g) SEM images of the NTP/rPGO-1; (e) SEM and (h) TEM images of the NTP/rPGO-2; and (f) SEM and (i) TEM images of the NTP/rPGO-3.

3. RESULTS AND DISCUSSION

3.1. Synthesis and Structural Characterization. Figure 1 illustrates the synthesis process of the NTP/rPGO composites. The PGO was prepared by the mild defect-etching reaction, and then assembled with the NTP precursor to produce the NTP/PGO by the hydrothermal reaction. After pyrolysis, the porous NTP/rPGO composites were obtained. The morphology of the synthesized samples is investigated by SEM and TEM. As displayed in Figure 2a,b, the rPGO flakes show a porous structure due to the defect-etching reaction. The wrinkled flakes of the graphene are interconnected to construct the 3D network. Herein, the rPGO sheets were expected to serve as a highly conductive substrate. Figure 2c shows the NTP nanoparticles with a narrow size range from 50 to 100 nm. The very regular shape (parallelepiped) implies the well-crystallized structure. As shown in Figure 2d–f, the NTP nanoparticles are well dispersed and attached by rPGO sheets in the NTP/rPGOs. Compared to the bare NTP, NTP nanoparticles in the NTP/rPGO show a smaller average particle size of ~60 nm. As shown in Figure 2g–i, the TEM images indicate that the NTP nanoparticles are uniformly attached on the rPGO sheets. They were closely anchored on the rPGO sheets. Interestingly, the hollow structure can be observed in some NTP particles. It is worth noting that such composite structure can increase the electrolyte/electrode contact area and facilitate the electronic and ionic transport.[42]

Figure 3a presents the XRD patterns of the NTP, rPGO, and NTP/rPGO. A broad diffraction peak at ~26° is found in the rPGO, corresponding to the typical (002) graphite plane (*d*-spacing value of 3.75 Å). The bare NTP exhibits some narrow diffraction peaks at 2θ = 14.52, 20.28, 20.98, 24.30, 29.30, and 36.68°, corresponding to (012), (104), (110), (113), (024), (116), and (300) planes of well-crystallized rhombohedral structure, respectively (space group: $R\bar{3}c$ (167), PDF no. 85-2265). After composting the rPGO, the NTP/rPGO composites display the same crystal phase. No peaks from other impurity phases are observed, suggesting that the NTP/rPGO composites are mainly made of the single $NaTi_2(PO_4)_3$ crystal phase. TGA analysis was carried out in the air to determine the amount of $NaTi_2(PO_4)_3$ in the composites (see Figure 3b). The major mass loss occurs at the onset temperature of 600 °C, and residual mass remains stable after 700 °C. Thus, the $NaTi_2(PO_4)_3$ amounts at 800 °C in the NTP/rPGO-1, NTP/rPGO-2, and NTP/rPGO-3 are calculated to be ~83, ~77, and ~74 wt %, respectively.

In addition, Raman spectra are obtained to confirm the carbide structure. As displayed in Figure 3c, two predominant peaks from the rPGO can be observed at 1340 and 1596 cm^{-1}, corresponding to the D (defeat) and G (graphite) bands, respectively. Compared to the bare rPGO, the lower intensity

DOI: 10.1021/acsomega.9b00984
ACS Omega 2019, 4, 11455−11463

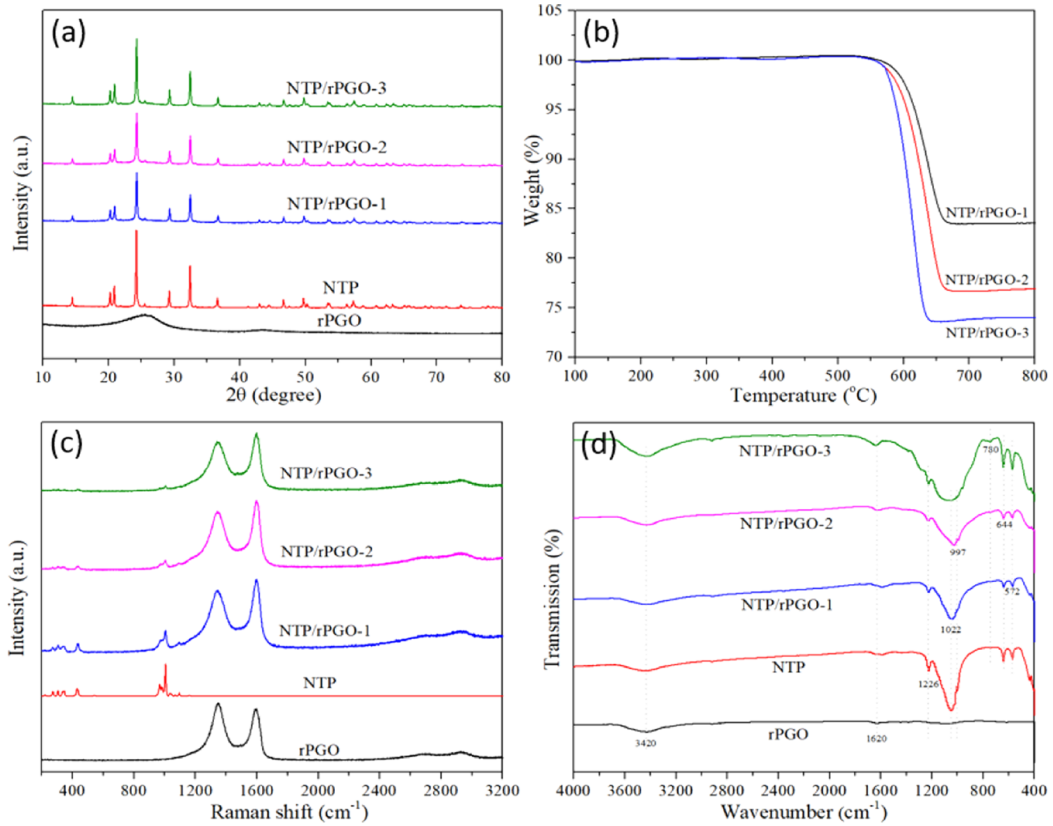

Figure 3. Structural characterization for the NTP, rPGO, and NTP/rPGOs: (a) XRD patterns, (b) TGA profiles, (c) Raman spectra, and (d) FTIR spectra.

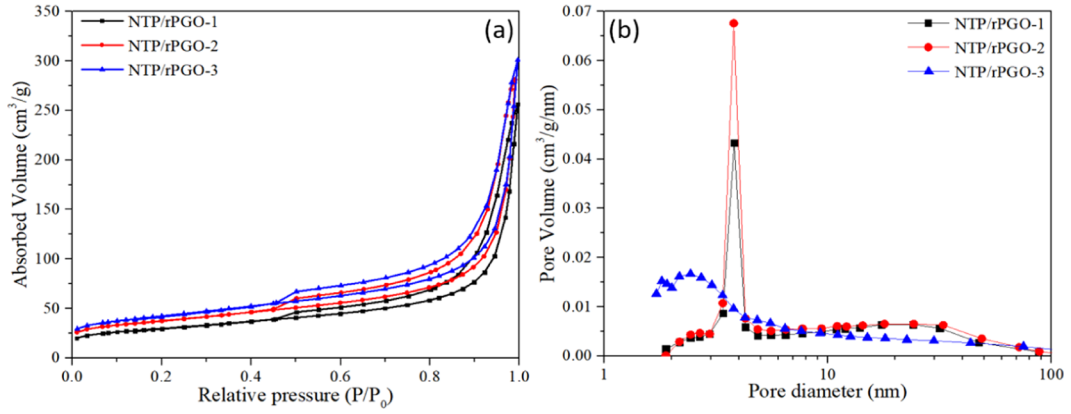

Figure 4. Porous structure of the NTP/rPGO-1, NTP/rPGO-2, and NTP/rPGO-3: (a) N_2 adsorption/desorption isotherms and (b) pore size distributions.

ratios of D band to G band (I_D/I_G) for NTP/rPGO suggest higher graphitization degree of composite carbon.[43] Besides, the bands at 990 and 1085 cm^{-1} are attributed to the characteristic symmetrical and asymmetrical stretching in the NTP lattice. The band at 272 cm^{-1} originates from the translational vibration of Ti^{4+} ions and those at 306, 341, and 438 cm^{-1} are associated with $(PO_4)^{3-}$.[44] The chemical composition of the synthesized composites is analyzed by FTIR measurement. In Figure 3d, the bands at 3420 and 1620 cm^{-1} are ascribed to the stretching and bending vibrations of O−H, which is from the residual hydroxyl groups in the rPGO sheets. The characteristic band at 1226 cm^{-1} is attributed to the stretching vibration of the PO_4 units. The bands at 1022 and 572 cm^{-1} are ascribed to the P−O bonds in the PO_4 tetrahedra, while the bands at 997 and 644 cm^{-1} correspond to the Ti−O−Ti bonds in the TiO_6 octahedra.[44] Interestingly, the NTP/rPGO composites display a new absorption band at 780 cm^{-1}, indicating the formation of the Ti−O−C chemical bond. Combined with morphology results, this finding confirms that the rPGO sheets and the NTP particles are successfully bonded together in the NTP/rPGO composites.

To determine the surface areas of porous composites, nitrogen adsorption−desorption isotherms were analyzed by semiempirical fitting. As displayed in Figure 4a, all of the isotherms exhibit typical IUPAC-IV isotherms (showing an obvious hysteresis loop) and high N_2 uptake, indicating a mesoporous structure. According to the BET method, the specific surface area of the NTP/rPGO-1, NTP/rPGO-2, and

DOI: 10.1021/acsomega.9b00984
ACS Omega 2019, 4, 11455−11463

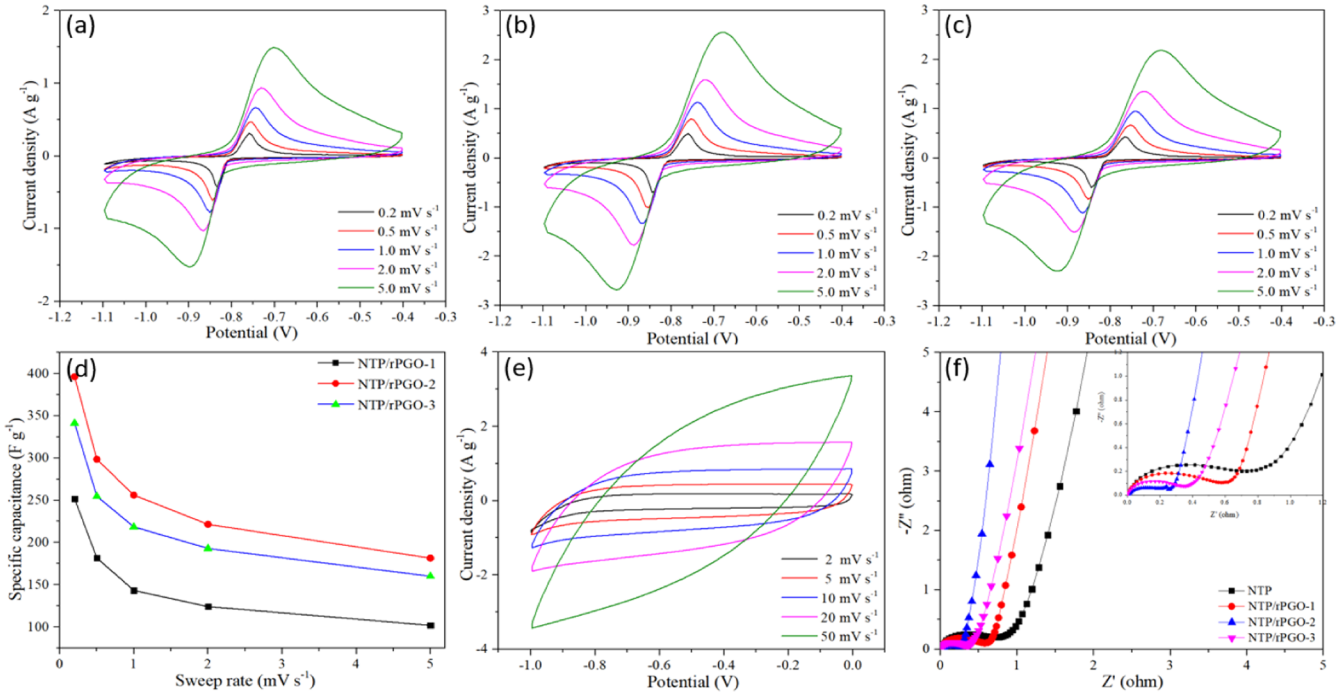

Figure 5. CV profiles at different scan rates: (a) NTP/rPGO-1, (b) NTP/rPGO-2, and (c) NTP/rPGO-3; (d) specific capacitances of the NTP/rPGO composites; (e) CV profile of AC at different scan rates; (f) EIS spectra of the NTP and NTP/rPGO composites.

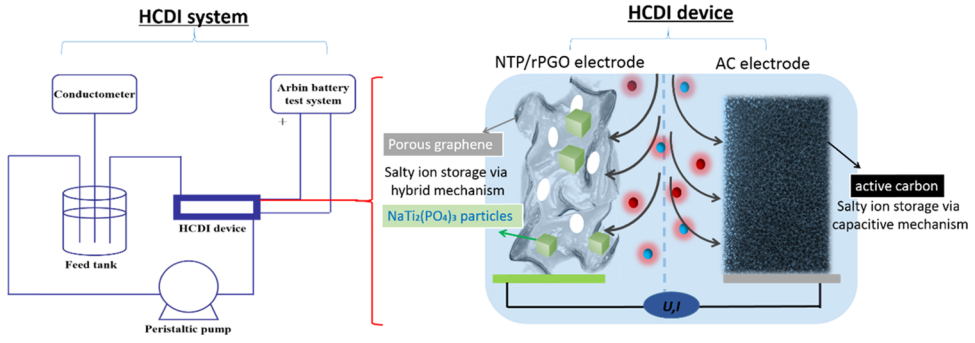

Figure 6. Schematic illustration of the HCDI system in this study, and the HCDI device is assembled using the NTP/rPGO electrode and the AC electrode.

NTP/rPGO-3 are calculated to be 102.68, 129.34, and 146.14 $m^2\ g^{-1}$, respectively.

The increase in the specific surface area is due to the high amount of porous rPGO. Figure 4b shows the pore size distribution calculated based on the Barrett–Joyner–Halenda method. The NTP/rPGO-1 and NTP/rPGO-2 show the narrow size distributions at around 4.1 nm and a broad one at around 24.0 nm. However, the pore size of NTP/rPGO-3 is mainly distributed at 2.4 nm, which is due to the predominance of the in-plane pores with the increase of the rPGO content. The overlapping pores size at 0.5–10.0 nm, to some extent, can enhance the desalination capacity.[45] Thus, the NTP/rPGO composites are appealing for the HCDI application.

3.2. Electrochemical Characterization and Deionization Test. To estimate the electrosorption performance, CV tests were performed here to obtain the capacity of the fabricated electrodes. Figure 5a–c displays the CV curves of the NTP/rPGO electrodes at varying scan rates from 0.2 to 5 mV s^{-1} in 1 M Na_2SO_4 aqueous electrolyte. At the scan rate of 0.2 mV s^{-1}, the redox peaks related to the deintercalation/intercalation reaction of Na^+ from/into the NTP/rPGOs are observed at −0.76 and −0.84 V, corresponding to the redox reaction of Ti^{4+}/Ti^{3+} in the NTP/rPGO electrode: $NaTi_2(PO_4)_3 + 2Na^+ + 2e^- \leftrightarrow Na_3Ti_2(PO_4)_3$. As the scan rates increase, the anodic and cathodic peaks move toward the lower and higher potentials, respectively. However, the peak intensity increases with a slight deviation with the increase in scan rate, indicating that the high cyclic stability, which agrees with the previous report.[46] Furthermore, the calculated specific capacities are displayed in Figure 5d. Among them, the NTP/rPGOs-2 electrode delivers high values at all scan rates. Typically, at the scan rate of 0.2 mV s^{-1}, the specific capacity of the NTP/rPGO-1, NTP/rPGO-2, and NTP/rPGO-3 are 251.78, 396.42, and 341.42 F g^{-1}, respectively. This is because the NTP/rPGO-2 has a higher specific surface area than that of the NTP/rPGO-1 and a wider mesoporous distribution than that of the NTP/rPGO-3. It not only increases the effective contact area between the electrode and electrolyte but also provides more active sites and short diffusion channels for ion transportation and storage, thus yielding a high specific capacity.[47] Here, as the negative electrode material in the

DOI: 10.1021/acsomega.9b00984
ACS Omega 2019, 4, 11455–11463

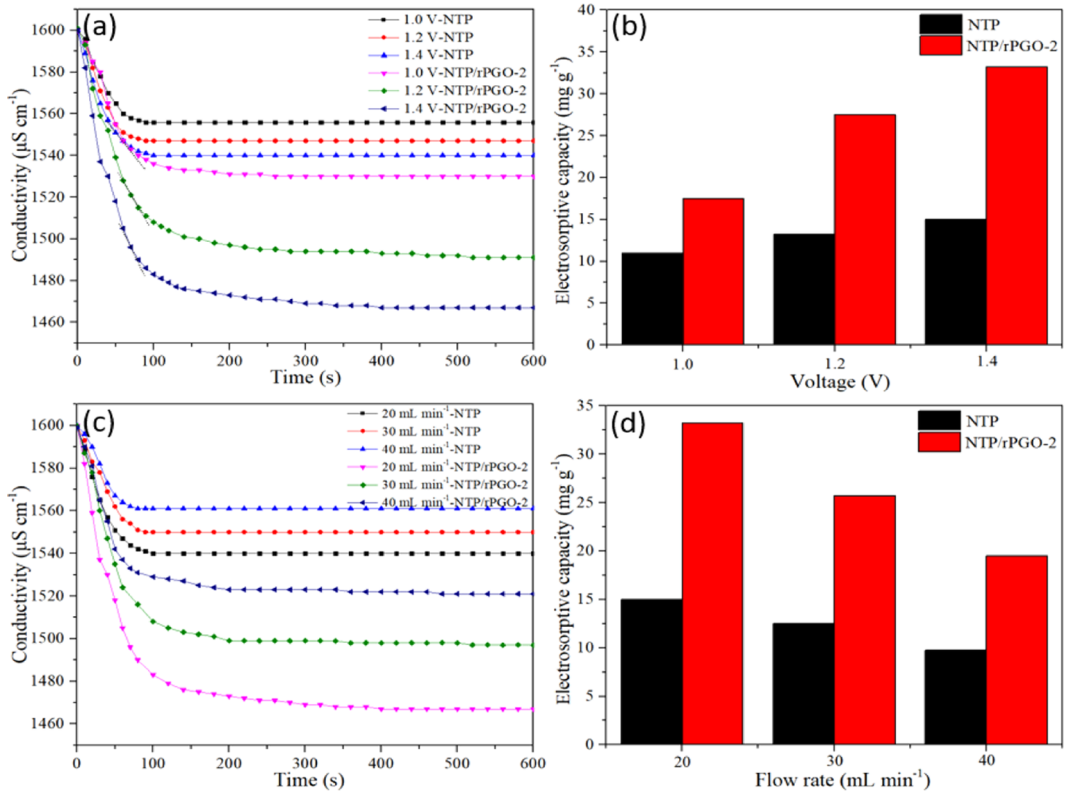

Figure 7. Influence of applied voltage: (a) the variation of the NaCl solution conductivity vs cycling time, and (b) the electrosorptive capacity of the NTP and NTP/rPGO-2 at different applied voltages. The influence of flow rate: (c) the curves of conductivity change vs time, and (d) the electrosorptive capacity of the NTP and NTP/rPGO-2 at different flow rates.

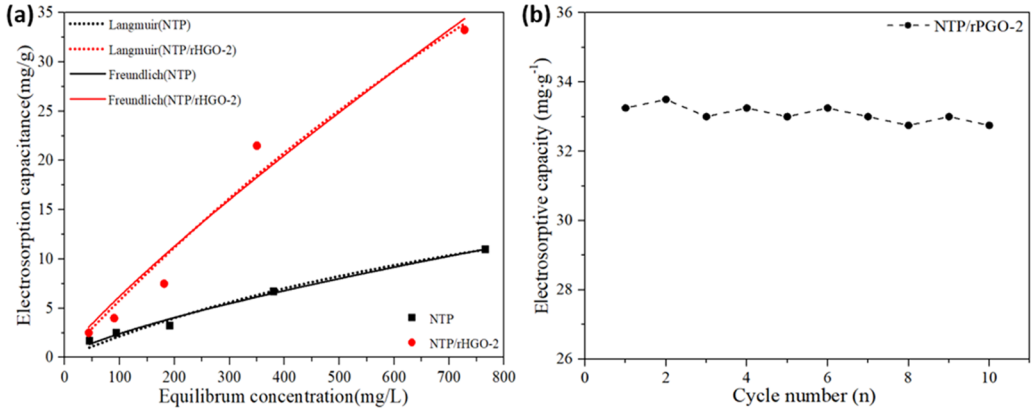

Figure 8. (a) Experimental and fitting data by employing Langmuir and Freundlich isotherms for the NTP and NTP/rPGO-2 and (b) the regeneration test of the NTP/rPGO-2 electrode.

Table 1. Parameters and Regression Coefficients R^2, k_L, and k_F of Langmuir and Freundlich Isotherms of the NTP and NTP/rPGO-2 at 25 °C

isotherm model	parameter	NTP	NTP/rPGO-2
Langmuir	q_m	28.4218	146.0301
	k_L	0.0008	0.0004
	R^2	0.9742	0.9654
Freundlich	k_F	0.0785	0.1179
	n	1.3437	1.1612
	R^2	0.9840	0.9993

HCDI cell, Figure 5e shows the CV curves of the AC in a potential window of −1.0−0 V (vs SCE). The approximately rectangular shape can be observed at the scan rates from 2 to 20 mV s^{-1}, which is a typical voltammogram for the EDL capacitor. Figure 5f gives EIS spectra of the NTP and NTP/rPGOs. The NTP/rPGO samples have a relatively low resistance than that of the NTP, i.e., the total resistance of the NTP is ∼0.8 Ω, whereas that of the NTP/rPGO-2 decreases to ∼0.3 Ω. This is ascribed to the fact that the rPGO provides favorable pathways for the ion transfer in the electrolyte and electrons in the electrode. Based on the superior performance mentioned above, the NTP/rPGO-2 was chosen as the positive electrode material in the HCDI system.

As illustrated in Figure 6, the batch-mode experiment for the HCDI system using the NTP|AC and the NTP/rPGO-2|AC was applied to compare their desalination performance. Figure

DOI: 10.1021/acsomega.9b00984
ACS Omega 2019, 4, 11455−11463

Table 2. Comparison of (H)CDI Performance of Various Types of Carbon Materials Using NaCl Solution in the Reports

sample	initial concentration (mg L^{-1})	applied voltage (V)	electrosorption capacity (mg g^{-1})	electrosorption rate (mg g^{-1} s^{-1})	refs
rGO/Co_3O_4	250	1.6	18.63	0.048	52
C@$Na_4Ti_9O_{20}$	1000	1.4	66.14		53
$Na_2FeP_2O_7$	585	1.2	30.20	0.081	54
$Na_4Mn_9O_{18}$	585	1.2	31.20		22
TiS_2/CNT	35100	0.8	35.80		55
$Mg_{0.14}MnO_2$	877.5	1.2	37.20		56
rGO/SnO_2/felt	400	1.2	17.62	∼0.01	57
ZrO_2/C	250	1.4	55.17	0.007	58
RuO_2(20)-AC	292	1.2	11.26		59
MnO_2	500	1.0	14.9		60
NTP/rPGO	786	1.4	33.25	0.30	this work

7a presents conductivity change vs cycling time of the NaCl solution with an initial concentration of 1600 μS cm^{-1} (786 mg L^{-1}) under 1.0, 1.2, and 1.4 V, respectively. There is a drastic decrease in conductivity at the beginning of the electrosorptive cycle due to large number of salt ions adsorbed here. As cycling time goes on, the conductivity tends to become constant because of the charge balance on the electrode surface. The adsorption rate of the NTP/rPGO-2|AC cell also increases with the increasing voltage (0.19, 0.23, and 0.30 mg g^{-1} s^{-1} at 1.0, 1.2, and 1.4 V, respectively), which is also evidenced by a rapid drop of the conductivity curves. It is noteworthy that such adsorption rate is 100 times higher than that of the bare graphene electrode.[48] Furthermore, the slope of the curve gradually increases as the applied voltage gradually increases. The average ion adsorption rates of the NTP/rPGO-2 and NTP were calculated to be 0.30 and 0.14 mg g^{-1} s^{-1} at 1.4 V, respectively. Figure 7b compares the electrosorptive capacity of the NTP with NTP/rPGO-2 at different voltages. The electrosorptive capacities of the NTP/rPGO-2 (i.e., 33.25 mg g^{-1} at 1.4 V) are twice as high as these of the bare NTP.

To investigate the influence of flow rate on the desalination performance, the flow rates were set to be 20, 30, and 40 mL min^{-1}, while 200 mL of NaCl solution (initial conductivity of 1600 μS cm^{-1} or initial concentration of 786 mg L^{-1}) was circularly pumped into HCDI cell under the constant voltage of 1.4 V. As shown in Figure 7c,d, the electrosorptive capacities of the NTP and NTP/rPGO-2 at 20 mL min^{-1} are 15 and 33.25 mg g^{-1}, respectively. The flow conductivity after reaching an electrosorption equilibrium becomes higher as the flow rate increases. Obviously, the high flow rate can result in a decrease in the desalination capacity, and this is because a low flow rate provides enough time for ion transport from a bulk flow to an electrode, especially at low current load.[49,50] When enlarging the flow rate, the shorter residence time for the unit volume of salt water inside the HCDI cell can result in a shorter time for the ions to migrate toward the electrodes. Thus, this ion-transport limitation decreases the electrosorptive capacity of the HCDI cell.

Beyond that, the NTP|AC and NTP/rPGO-2|AC cells were also performed in the NaCl solution with various concentrations to reveal the relationship between desalination capacity and initial conductivity. Figure 8a presents the electrosorption capacitance vs equilibrium concentration. The result implies that the higher initial conductivity can lead to a higher removal amount of salt ions. The experimental data can be fitted by applying the Langmuir model (eq 3) and the Freundlich model (eq 4) for the NTP|AC and NTP/rPGO-2|AC system, respectively[51]

$$q_e = q_m K_L C_e/(1 + K_L C_e) \quad (3)$$

$$q_e = k_F C_e^{1/n} \quad (4)$$

where q_e (mg g^{-1}) is the amount of removed NaCl, C_e is the equilibrium concentration (mg L^{-1}), and q_m (mg g^{-1}) is the maximum desalination capacity corresponding to the complete monolayer coverage, and n is an empirical constant. k_L and k_F are the Langmuir constant and the Freundlich constant, respectively. The parameters of Langmuir and Freundlich models and regression coefficients are listed in Table 1. Based on the regression coefficient (R^2), the Freundlich model fits the experimental data of the NTP/rPGO-2 better than the Langmuir model does. Thus, this indicates that the multilayer absorption is the main adsorption mechanism for the NTP and NTP/rPGO-2 electrodes during the electrosorption process. In general, the Langmuir model and the Freundlich model are used in the chemical adsorption and physical/chemical adsorption, respectively. The electrosorption behavior of the NTP/rPGO-2 confirms the hybrid adsorption. Additionally, the regeneration test on the NTP/rPGO-2 electrode was performed using the NaCl solution with an initial conductivity of 1600 μS cm^{-1} (786 mg L^{-1}) under the applied voltage of 1.4 V. As shown in Figure 8b, the electrosorptive capacity of the HCDI system remains almost unchanged (∼33 mg g^{-1}) in the initial ten electrosorption/desorption cycles. This stable behavior is ascribed to the stable 3D porous structure of the NTP/rPGO, which can not only prevent the aggregation of the NTP nanoparticles but also offer continuous ion/electron pathway during the electrochemical salt removal process. This further confirms that the NTP/rPGO-2 is a promising HCDI electrode material.

Compared to previous reports (see Table 2), the electrosorption capacity of the NTP/rPGO-2 obtained in this study is acceptable based on the initial NaCl concentration of 786 mg L^{-1}. It is noteworthy that the electrosorption rate of the NTP/rPGO-2 electrode (0.3 mg g^{-1} s^{-1}) is superior. In sum, the superior desalination performances of the NTP/rPGO can be attributed to the following reasons: (1) the 3D porous graphene matrix with a high surface area and abundant channels results in a fast salt ion migration and a high capacitive storage; (2) the nanosized NTP loaded on the graphene matrix can boost the reversible capacity and desalination capability, while the large open space in the graphene matrix can accommodate the volume variation of the NTP during the desalination process. Thus, this hybrid electrode used in the HCDI system can lead to high ion removal capacity and rate.

DOI: 10.1021/acsomega.9b00984
ACS Omega 2019, 4, 11455−11463

4. CONCLUSIONS

In this study, we prepare a series of the NTP/rPGO composites through assembling the NTP precursor with porous graphene oxide by hydrothermal method followed by carbonization treatment. Inside the composites, the NTP particles are uniformly dispersed and attached on the rPGO sheets, the latter serve as a conductive substrate. The synthesized NTP/rPGO composites are employed as an electrode for the HCDI system. The HCDI cell based on the NTP/rPGO-2|AC shows a high desalination capacity of 33.25 mg g^{-1} at an applied potential of 1.4 V with an initial salt conductivity of 1600 μS cm^{-1} (786 mg L^{-1}). This is because the dispersed NTP nanoparticles provide abundant sites for ion adsorption based on the redox reaction. Furthermore, the rPGO sheets construct a conductive 3D network, resulting in a high capacitive storage and a low transient resistivity. Therefore, a rapid ion removal rate of 0.3 mg g^{-1} s^{-1} has been achieved due to the hybrid electrodes and porous structure. Combining with the excellent regeneration ability, the NTP/rPGO composites exhibit promising properties as an electrode material for seawater desalination in the future.

AUTHOR INFORMATION

Corresponding Authors

*E-mail: qhmeng@mail.buct.edu.cn. Tel/Fax: +86 1064436876 (Q.M.).

*E-mail: guiying.tian@partner.kit.edu. Tel: +49 72160828505 (G.T.).

ORCID

Guiying Tian: 0000-0002-7791-3479

Notes

The authors declare no competing financial interest.

ACKNOWLEDGMENTS

It is a pleasure to acknowledge the financial support of this research by the National Natural Science Foundation of China (51372011) and the China Scholarship Council (201506880029).

REFERENCES

(1) Tang, W.; Liang, J.; He, D.; Gong, J.; Tang, L.; Liu, Z.; Wang, D.; Zeng, G. Various Cell Architectures of Capacitive Deionization: Recent Advances and Future Trends. *Water Res.* **2019**, *150*, 225−251.

(2) Service, R. F. Desalination Freshens Up. *Science* **2006**, *313*, 1088−1090.

(3) Peñate, B.; García-Rodríguez, L. Current Trends and Future Prospects in the Design of Seawater Reverse Osmosis Desalination Technology. *Desalination* **2012**, *284*, 1−8.

(4) Camacho, L. M.; Dumée, L.; Zhang, J.; Li, J.-d.; Duke, M.; Gomez, J.; Gray, S. Advances in Membrane Distillation for Water Desalination and Purification Applications. *Water* **2013**, *5*, 94−196.

(5) Phillip, W. A.; Elimelech, M. The Future of Seawater Desalination: Energy, Technology, and the Environment. *Science* **2011**, *333*, 712−717.

(6) Porada, S.; Zhao, R.; Van Der Wal, A.; Presser, V.; Biesheuvel, P. M. Review on the Science and Technology of Water Desalination by Capacitive Deionization. *Prog. Mater. Sci.* **2013**, *58*, 1388−1442.

(7) Suss, M. E.; Porada, S.; Sun, X.; Biesheuvel, P. M.; Yoon, J.; Presser, V. Water Desalination via Capacitive Deionization: What Is It and What Can We Expect from It? *Energy Environ. Sci.* **2015**, *8*, 2296−2319.

(8) Anderson, M. A.; Cudero, A. L.; Palma, J. Capacitive Deionization as an Electrochemical Means of Saving Energy and Delivering Clean Water. Comparison to Present Desalination Practices: Will It Compete? *Electrochim. Acta* **2010**, *55*, 3845−3856.

(9) Bouhadana, Y.; Avraham, E.; Noked, M.; Ben-Tzion, M.; Soffer, A.; Aurbach, D. Capacitive Deionization of NaCl Solutions at Non-Steady-State Conditions: Inversion Functionality of the Carbon Electrodes. *J. Phys. Chem. C* **2011**, *115*, 16567−16573.

(10) Barbieri, O.; Hahn, M.; Herzog, A.; Kötz, R. Capacitance Limits of High Surface Area Activated Carbons for Double Layer Capacitors. *Carbon* **2005**, *43*, 1303−1310.

(11) Li, L.; Zou, L.; Song, H.; Morris, G. Ordered Mesoporous Carbons Synthesized by a Modified Sol-Gel Process for Electrosorptive Removal of Sodium Chloride. *Carbon* **2009**, *47*, 775−781.

(12) Soffer, A.; Aurbach, D.; Noked, M.; Bouhadana, Y.; Avraham, E. Limitations of Charge Efficiency in Capacitive Deionization. *J. Electrochem. Soc.* **2009**, *156*, P157.

(13) El-Deen, A. G.; Choi, J. H.; Kim, C. S.; Khalil, K. A.; Almajid, A. A.; Barakat, N. A. M. TiO_2 Nanorod-Intercalated Reduced Graphene Oxide as High Performance Electrode Material for Membrane Capacitive Deionization. *Desalination* **2015**, *361*, 53−64.

(14) Biesheuvel, P. M.; van der Wal, A. Membrane Capacitive Deionization. *J. Membr. Sci.* **2010**, *346*, 256−262.

(15) Qian, B.; Wang, G.; Ling, Z.; Dong, Q.; Wu, T.; Zhang, X.; Qiu, J. Sulfonated Graphene as Cation-Selective Coating: A New Strategy for High-Performance Membrane Capacitive Deionization. *Adv. Mater. Interfaces* **2015**, *2*, No. 1500372.

(16) Jeon, S.-i.; Park, H. R.; Yeo, J. G.; Yang, S.; Cho, C. H.; Han, M. H.; Kim, D. K. Desalination via a New Membrane Capacitive Deionization Process Utilizing Flow-Electrodes. *Energy Environ. Sci.* **2013**, *6*, 1471−1475.

(17) Presser, V.; Weingarth, D.; Bryjak, M.; Biesheuvel, P. M.; Porada, S.; Hamelers, H. V. M. Carbon Flow Electrodes for Continuous Operation of Capacitive Deionization and Capacitive Mixing Energy Generation. *J. Mater. Chem. A* **2014**, *2*, 9313.

(18) Gao, X.; Omosebi, A.; Landon, J.; Liu, K. Enhanced Salt Removal in an Inverted Capacitive Deionization Cell Using Amine Modified Microporous Carbon Cathodes. *Environ. Sci. Technol.* **2015**, *49*, 10920−10926.

(19) Gao, X.; Omosebi, A.; Landon, J.; Liu, K. Surface Charge Enhanced Carbon Electrodes for Stable and Efficient Capacitive Deionization Using Inverted Adsorption−Desorption Behavior. *Energy Environ. Sci.* **2015**, *8*, 897−909.

(20) Logan, B. E.; La Mantia, F.; Pasta, M.; Cui, Y.; Deshazer, H. D. Batteries for Efficient Energy Extraction from a Water Salinity Difference. *Nano Lett.* **2011**, *11*, 1810−1813.

(21) Pasta, M.; Wessells, C. D.; Cui, Y.; La Mantia, F. A Desalination Battery. *Nano Lett.* **2012**, *12*, 839−843.

(22) Lee, J.; Kim, S.; Kim, C.; Yoon, J. Hybrid Capacitive Deionization to Enhance the Desalination Performance of Capacitive Techniques. *Energy Environ. Sci.* **2014**, *7*, 3683−3689.

(23) Wang, G.; Zhang, L.; Zhang, J. A Review of Electrode Materials for Electrochemical Supercapacitors. *Chem. Soc. Rev.* **2012**, *41*, 797−828.

(24) Li, H.; Pan, L.; Nie, C.; Liu, Y.; Sun, Z. Reduced Graphene Oxide and Activated Carbon Composites for Capacitive Deionization. *J. Mater. Chem.* **2012**, *22*, 15556−15561.

(25) Dong, Q.; Qiu, J.; Wang, G.; Ling, Z.; Yu, C.; Pan, C. Hierarchical Activated Carbon Nanofiber Webs with Tuned Structure Fabricated by Electrospinning for Capacitive Deionization. *J. Mater. Chem.* **2012**, *22*, 21819.

(26) El-Deen, A. G.; Boom, R. M.; Kim, H. Y.; Duan, H.; Chan-Park, M. B.; Choi, J. H. Flexible 3D Nanoporous Graphene for Desalination and Bio-Decontamination of Brackish Water via Asymmetric Capacitive Deionization. *ACS Appl. Mater. Interfaces* **2016**, *8*, 25313−25325.

(27) Xu, P.; Drewes, J. E.; Heil, D.; Wang, G. Treatment of Brackish Produced Water Using Carbon Aerogel-Based Capacitive Deionization Technology. *Water Res.* **2008**, *42*, 2605−2617.

DOI: 10.1021/acsomega.9b00984
ACS Omega 2019, 4, 11455−11463

(28) Li, H.; Liang, S.; Li, J.; He, L. The Capacitive Deionization Behaviour of a Carbon Nanotube and Reduced Graphene Oxide Composite. *J. Mater. Chem. A* **2013**, *1*, 6335−6341.
(29) Wimalasiri, Y.; Zou, L. Carbon Nanotube/Graphene Composite for Enhanced Capacitive Deionization Performance. *Carbon* **2013**, *59*, 464−471.
(30) Shi, L.; Zhang, J.; Zhang, D.; Yan, T.; Lei, H.; Wang, H. Graphene-like Carbon Nanosheets Prepared by a Fe-Catalyzed Glucose-Blowing Method for Capacitive Deionization. *J. Mater. Chem. A* **2015**, *3*, 5934−5941.
(31) Yin, H.; Zhao, S.; Wan, J.; Tang, H.; Chang, L.; He, L.; Zhao, H.; Gao, Y.; Tang, Z. Three-Dimensional Graphene/Metal Oxide Nanoparticle Hybrids for High-Performance Capacitive Deionization of Saline Water. *Adv. Mater.* **2013**, *25*, 6270−6276.
(32) Xu, X.; Pan, L.; Liu, Y.; Lu, T.; Sun, Z.; Chua, D. H. C. Facile Synthesis of Novel Graphene Sponge for High Performance Capacitive Deionization. *Sci. Rep.* **2015**, *5*, No. 8458.
(33) Zoromba, M. S.; Abdel-Aziz, M. H.; Bassyouni, M.; Gutub, S.; Demko, D.; Abdelkader, A. Electrochemical Activation of Graphene at Low Temperature: The Synthesis of Three-Dimensional Nano-architectures for High Performance Supercapacitors and Capacitive Deionization. *ACS Sustainable Chem. Eng.* **2017**, *5*, 4573−4581.
(34) Yoon, H.; Lee, J.; Kim, S.; Yoon, J. Hybrid Capacitive Deionization with Ag Coated Carbon Composite Electrode. *Desalination* **2017**, *422*, 42−48.
(35) Divyapriya, G.; Vijayakumar, K. K.; Nambi, I. Development of a Novel Graphene/Co_3O_4 composite for Hybrid Capacitive Deionization System. *Desalination* **2019**, *451*, 102−110.
(36) Zhou, F.; Gao, T.; Luo, M.; Li, H. Heterostructured Graphene@$Na_4Ti_9O_{20}$ Nanotubes for Asymmetrical Capacitive Deionization with Ultrahigh Desalination Capacity. *Chem. Eng. J.* **2018**, *343*, 8−15.
(37) Huang, Y.; Chen, F.; Guo, L.; Yang, H. Y. Ultrahigh Performance of a Novel Electrochemical Deionization System Based on a $NaTi_2(PO_4)_3$/RGO Nanocomposite. *J. Mater. Chem. A* **2017**, *5*, 18157−18165.
(38) Xu, C.; Xu, B.; Gu, Y.; Xiong, Z.; Sun, J.; Zhao, X. S. Graphene-Based Electrodes for Electrochemical Energy Storage. *Energy Environ. Sci.* **2013**, *6*, 1388−1414.
(39) Xu, Y.; Chen, C. Y.; Zhao, Z.; Lin, Z.; Lee, C.; Xu, X.; Wang, C.; Huang, Y.; Shakir, M. I.; Duan, X. Solution Processable Holey Graphene Oxide and Its Derived Macrostructures for High-Performance Supercapacitors. *Nano Lett.* **2015**, *15*, 4605−4610.
(40) Marcano, D. C.; Kosynkin, D. V.; Berlin, J. M.; Sinitskii, A.; Sun, Z.; Slesarev, A.; Alemany, L. B.; Lu, W.; Tour, J. M. Improved Synthesis of Graphene Oxide. *ACS Nano* **2010**, *4*, 4806−4814.
(41) Tian, G.; Liu, L.; Meng, Q.; Cao, B. Preparation and Characterization of Cross-Linked Quaternised Polyvinyl Alcohol Membrane/Activated Carbon Composite Electrode for Membrane Capacitive Deionization. *Desalination* **2014**, *354*, 107−115.
(42) Roh, H. K.; Kim, H. K.; Kim, M. S.; Kim, D. H.; Chung, K. Y.; Roh, K. C.; Kim, K. B. In Situ Synthesis of Chemically Bonded $NaTi_2(PO_4)_3$/RGO 2D Nanocomposite for High-Rate Sodium-Ion Batteries. *Nano Res.* **2016**, *9*, 1844−1855.
(43) Tuinstra, F.; Koenig, J. L. Characterization of Graphite Fiber Surfaces with Raman Spectroscopy. *J. Compos. Mater.* **1970**, *4*, 492−499.
(44) Roh, H.-K.; Kim, M.-S.; Chung, K. Y.; Ulaganathan, M.; Aravindan, V.; Madhavi, S.; Roh, K. C.; Kim, K.-B. A Chemically Bonded $NaTi_2(PO_4)_3$/RGO Microsphere Composite as a High-Rate Insertion Anode for Sodium-Ion Capacitors. *J. Mater. Chem. A* **2017**, *5*, 17506−17516.
(45) Zhi, J.; Wang, Y.; Deng, S.; Hu, A. Study on the Relation between Pore Size and Supercapacitance in Mesoporous Carbon Electrodes with Silica-Supported Carbon Nanomembranes. *RSC Adv.* **2014**, *4*, 40296−40300.
(46) Li, Z.; Young, D.; Xiang, K.; Carter, W. C.; Chiang, Y. M. Towards High Power High Energy Aqueous Sodium-Ion Batteries: The $NaTi_2(PO_4)_3/Na_{0.44}MnO_2$ system. *Adv. Energy Mater.* **2013**, *3*, 290−294.
(47) Zhang, L.; Wang, X.; Deng, W.; Zang, X.; Liu, C.; Li, C.; Chen, J.; Xue, M.; Li, R.; Pan, F. An Open Holey Structure Enhanced Rate Capability in a $NaTi_2(PO_4)_3$/C Nanocomposite and Provided Ultralong-Life Sodium-Ion Storage. *Nanoscale* **2018**, *10*, 958−963.
(48) Ma, J.; Wang, L.; Yu, F. Water-Enhanced Performance in Capacitive Deionization for Desalination Based on Graphene Gel as Electrode Material. *Electrochim. Acta* **2018**, *263*, 40−46.
(49) Kim, T.; Yoon, J. CDI Ragone Plot as a Functional Tool to Evaluate Desalination Performance in Capacitive Deionization. *RSC Adv.* **2015**, *5*, 1456−1461.
(50) Xu, Q.; Zhao, T. S.; Zhang, C. Performance of a Vanadium Redox Flow Battery with and without Flow Fields. *Electrochim. Acta* **2014**, *142*, 61−67.
(51) Wang, Z.; Dou, B.; Zheng, L.; Zhang, G.; Liu, Z.; Hao, Z. Effective Desalination by Capacitive Deionization with Functional Graphene Nanocomposite as Novel Electrode Material. *Desalination* **2012**, *299*, 96−102.
(52) Divyapriya, G.; Vijayakumar, K. K.; Nambi, I. Development of a Novel Graphene/Co_3O_4 Composite for Hybrid Capacitive Deionization System. *Desalination* **2019**, *451*, 102−110.
(53) Yue, Z.; Gao, T.; Li, H. Robust Synthesis of Carbon@$Na_4Ti_9O_{20}$ Core-Shell Nanotubes for Hybrid Capacitive Deionization with Enhanced Performance. *Desalination* **2019**, *449*, 69−77.
(54) Kim, S.; Lee, J.; Kim, C.; Yoon, J. $Na_2FeP_2O_7$ as a Novel Material for Hybrid Capacitive Deionization. *Electrochim. Acta* **2016**, *203*, 265−271.
(55) Srimuk, P.; Lee, J.; Tolosa, A.; Kim, C.; Aslan, M.; Presser, V. Titanium Disulfide: A Promising Low-Dimensional Electrode Material for Sodium Ion Intercalation for Seawater Desalination. *Chem. Mater.* **2017**, *29*, 9964−9973.
(56) Byles, B. W.; Hayes-Oberst, B.; Pomerantseva, E. Ion Removal Performance, Structural/Compositional Dynamics, and Electrochemical Stability of Layered Manganese Oxide Electrodes in Hybrid Capacitive Deionization. *ACS Appl. Mater. Interfaces* **2018**, *10*, 32313−32322.
(57) Sami, S. K.; Seo, J. Y.; Hyeon, S. E.; Shershah, M. S. A.; Yoo, P. J.; Chung, C. H. Enhanced Capacitive Deionization Performance by an RGO-SnO_2 Nanocomposite Modified Carbon Felt Electrode. *RSC Adv.* **2018**, *8*, 4182−4190.
(58) Yang, S.; Luo, M. In-Situ Embedding ZrO_2 Nanoparticles in Hierarchically Porous Carbon Matrix as Electrode Materials for High Desalination Capacity of Hybrid Capacitive Deionization. *Mater. Lett.* **2019**, *248*, 197−200.
(59) Ma, X.; Chen, Y. A.; Zhou, K.; Wu, P. C.; Hou, C. H. Enhanced Desalination Performance via Mixed Capacitive-Faradaic Ion Storage Using RuO_2-Activated Carbon Composite Electrodes. *Electrochim. Acta* **2019**, *295*, 769−777.
(60) Wu, T.; Wang, G.; Wang, S.; Zhan, F.; Fu, Y.; Qiao, H.; Qiu, J. Highly Stable Hybrid Capacitive Deionization with a MnO_2 Anode and a Positively Charged Cathode. *Environ. Sci. Technol. Lett.* **2018**, *5*, 98−102.

DOI: 10.1021/acsomega.9b00984
ACS Omega 2019, 4, 11455−11463